nature communications

Article

https://doi.org/10.1038/s41467-025-57939-8

Hydrogen-bonded organic frameworks for photocatalytic synthesis of hydrogen peroxide

Received: 7 September 2024

Accepted: 7 March 2025

Published online: 12 March 2025

Check for updates

Ji-Hong Zhang[1,2], Zhao-Ming Ge[1,2], Juan Wang[1], Di-Chang Zhong[1] ✉ & Tong-Bu Lu[1]

Photocatalysis provides a sustainable and environment-friendly strategy to produce H_2O_2, yet the catalytic efficiency of H_2O_2 overall photosynthesis ($O_2 + 2H_2O \rightarrow 2H_2O_2$) needs to be further improved, especially in the absence of additional cocatalysts, photosensitizers and sacrificial agents. Here we find that hydrogen-bonded organic frameworks can serve as photocatalysts for H_2O_2 overall photosynthesis under the above-mentioned conditions. Specifically, we constructed a donor–acceptor hydrogen-bonded organic framework that exhibits a high photocatalytic activity for H_2O_2 overall photosynthesis, with a production rate of 681.2 μmol g^{-1} h^{-1}. The control experiments and theoretical calculation revealed that the hydrogen-bonded organic frameworks with donor–acceptor structures can not only accelerate the charge separation and transfer but also optimize the reaction pathways, which significantly boosts the photocatalytic efficiency in H_2O_2 overall photosynthesis. This work provides insights into the design and development of efficient photocatalysts for overall H_2O_2 photosynthesis.

Hydrogen peroxide (H_2O_2) is a crucial chemical with broad applications spanning various industrial processes, including bleaching, pulping, disinfection, environmental remediation[1–6]. To date, the typical technology for industrial H_2O_2 production is the anthraquinone method, which utilizes Pd-catalyzed cyclic hydrogenation and oxidation of alkyl-anthraquinones in organic solvents[7–9]. This method comes with energy and environmental issues owing to substantial energy consumption and the formation of hazardous organic wastes[10,11]. Therefore, it is essential to develop alternative, economical and environmentally sustainable approaches to H_2O_2 synthesis.

Photocatalysis, utilizing visible light as an energy source, is regarded as a sustainable and environment-friendly strategy to replace the conventional route for H_2O_2 production[4,12–16]. Many photocatalysts, such as graphitic carbon nitride (g-C_3N_4), metal–organic frameworks (MOFs), covalent-organic frameworks (COFs), and organic polymers, have been used in H_2O_2 photosynthesis[17–29]. However, the photocatalytic efficiency for H_2O_2 production needs to be further improved. Although using sacrificial agents could effectively improve the photocatalytic efficiency, it would render the catalytic systems less economical. The development of advanced photocatalytic systems without additional sacrificial agents, that is, overall photosynthesis of H_2O_2 ($O_2 + 2H_2O \rightarrow 2H_2O_2$) from both O_2 reduction and H_2O oxidation, is urgently needed. Theoretically, the half-reaction of O_2 reduction could be readily achieved, as the LUMO positions of most photocatalysts are more negative than the theoretical oxygen reduction potential (H_2O_2/O_2, 0.28 V versus NHE, pH=7)[29]. In contrast, it is more challenging to achieve the half-reaction of H_2O oxidation, as the H_2O oxidation could undergo either a two-electron transfer process to produce H_2O_2 (1.38 V versus NHE, pH = 7) or a four-electron transfer process to produce O_2 (0.82 V versus NHE, pH = 7), and the latter is thermodynamically favorable in spite of a higher kinetic energy barrier because of more electrons and protons transfer involved. It is therefore unsurprising that only a few photocatalysts have achieved the overall photosynthesis of H_2O_2 via $2e^-$ O_2 reduction and $2e^-$ H_2O oxidation processes simultaneously[12,22,26].

[1]Institute for New Energy Materials and Low Carbon Technologies, School of Materials Science and Engineering, Tianjin University of Technology, Tianjin 300384, China. [2]These authors contributed equally: Ji-Hong Zhang, Zhao-Ming Ge. ✉e-mail: dczhong@email.tjut.edu.cn

Hydrogen-bonded organic frameworks (HOFs) are a type of emerging porous crystalline materials assembled by organic molecules linked through hydrogen bonds and other intermolecular interactions[30–32]. Assembled by weak intermolecular interactions, most HOFs show lower stabilities than MOFs and COFs, in which the structural units are connected by coordination/covalent bonds. However, besides hydrogen bonds, the π−π stacking interactions, electrostatic interactions, and framework interpenetration can synergistically strengthen the stability of HOFs[33–39]. Moreover, HOFs offer notable advantages, including low toxicity, mild synthesis, solution processability, and facile regeneration or healing by simple recrystallization. These features enable HOFs to show extensive applications in gas storage and separation, proton conduction, heterogeneous catalysis, biotechnology, medicine, and so on[31,32,40–43]. In particular, recent studies have revealed that the π−π stacking interactions can serve as channels to accelerate the electron transfer[44,45], which further extends the potential applications of HOFs in photocatalysis, encompassing hydrogen evolution, CO_2 reduction, and organic pollutant degradation[32,46–50]. However, HOFs as photocatalysts for H_2O_2 synthesis have not been reported thus far.

Donor–acceptor structures, comprising electron-rich donor units and electron-deficient acceptor units, have been reported to facilitate the charge transfer from the donor to the acceptor. The electronic pull–push effect between the donor and acceptor units can greatly promote the separation and transfer of photogenerated electrons and holes[51–54]. With the above consideration in mind, we have been devoted to developing donor–acceptor HOFs to boost the overall photosynthesis of H_2O_2. Herein, we report that the construction of donor–acceptor HOF could greatly increase the catalytic efficiency of H_2O_2 overall photosynthesis from H_2O and O_2 (Fig. 1a). Specifically, we selected tetrathiafulvalene tetracarboxylic acid (TTF) as the electron-donating unit and 4,4′-bipydine (Bpy) as the electron-accepting unit. Using the hydrogen bonds between them, a donor–acceptor HOF (denoted as TTF-Bpy-HOF) was constructed. For comparison, a HOF (TTF-HOF) based on the hydrogen bonds between TTF molecules was also constructed. We found that the TTF-HOF can simultaneously catalyze H_2O_2 synthesis via O_2 reduction and H_2O oxidation, with a rate of 74.4 μmol g^{-1} h^{-1} in the absence of any additional cocatalysts, photosensitizers, and sacrificial agents. More impressively, after the introduction of the acceptor moiety Bpy, the TTF-Bpy-HOF exhibits a remarkably enhanced H_2O_2 generation rate of 681.2 μmol g^{-1} h^{-1}, over 9 times higher than that of TTF-HOF. The photocatalytic and electron paramagnetic resonance (EPR) trapping experiments revealed that the Bpy units optimized the reaction paths for O_2 reduction. Moreover, the donor–acceptor structure can promote charge separation and transfer, thus greatly boosting the catalytic activity of H_2O_2 overall photosynthesis. This work provides insights for the design and development of efficient photocatalysts for overall photosynthesis of H_2O_2 from H_2O and O_2.

Results

Preparation and structure determination

The TTF-HOF and TTF-Bpy-HOF catalysts were synthesized according to the methods previously reported (Fig. 1a and Supplementary Table 1)[55,56]. The crystal structure of TTF-HOF shows that each TTF molecule is connected to four equivalent molecules through dimeric O–H···O hydrogen bonds ($D_{O...O}$ = 2.64 Å) between the carboxylic groups of adjacent TTF molecules, resulting in a two-dimensional (2D) layer with rhombus pores (Fig. 1b). The adjacent 2D layers further stack together through AA mode, forming a 3D porous supramolecular structure with rhombus channels. The channel size is measured to be 9.3 × 7.2 $Å^2$ (Supplementary Fig. 1). Upon the introduction of Bpy, the dimeric O–H···O hydrogen bonds are disrupted[57]. Instead, two types of hydrogen bonds contributing to the formation of TTF-Bpy-HOF are present (Fig. 1c). One is the O–H···N hydrogen bond between the carboxylic group and pyridyl moiety ($D_{O...N}$ = 2.63 Å), and the other is the O–H···O hydrogen bond ($D_{O...O}$ = 2.56 Å) between the carboxylic groups. Through these hydrogen bond interactions, TTF and Bpy are linked, forming a 2D supramolecular layer with two types of pores (Fig. 1c). Each 2D supramolecular layer further stacks with adjacent layers through π−π stacking interactions, generating a 3D porous supramolecular framework with 1D channels of 8.0 × 4.3 $Å^2$ (Supplementary Fig. 2). The morphology and compositions of TTF-HOF and TTF-Bpy-HOF were characterized by scanning electron microscopy (SEM), Fourier transform infrared (FTIR) spectroscopy and X-ray photoelectron spectroscopy (XPS) (Supplementary Figs. 3–12). SEM images show that TTF-HOF and TTF-Bpy-HOF have a similar cuboid morphology (Supplementary Fig. 4). The powder X-ray diffraction patterns for TTF-HOF and TTF-Bpy-HOF agree well with the simulated ones from their single crystal data (Supplementary Figs. 5 and 6)[55,56].

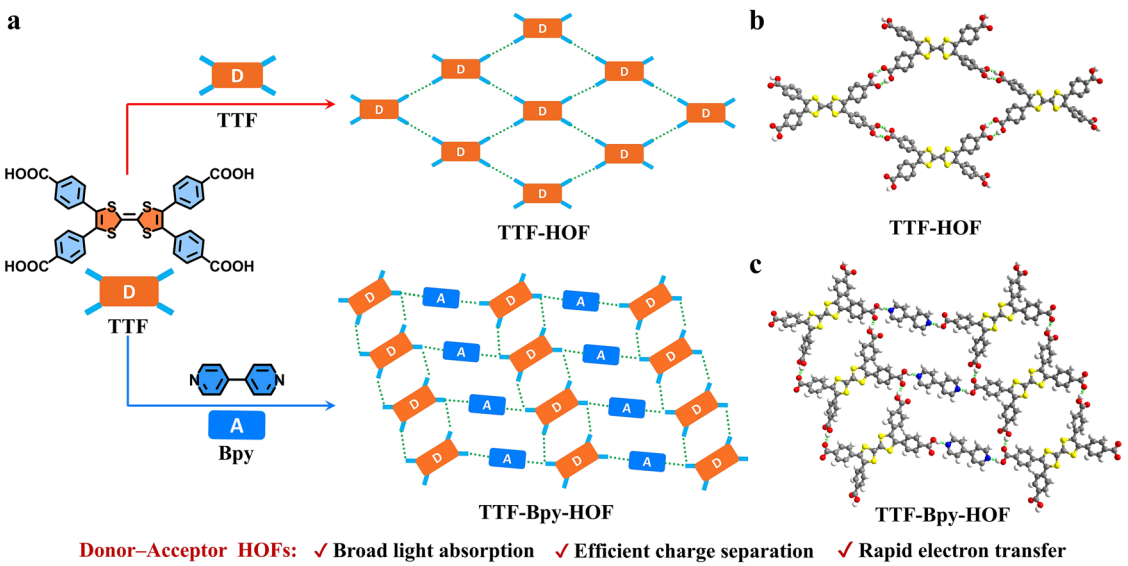

Fig. 1 | Schematic illustration. a Schematically showing the structures of general HOF (TTF-HOF) and donor-acceptor HOF (TTF-Bpy-HOF); crystal structures of **b** TTF-HOF stabilized by dimeric O-H…O hydrogen bonds with the O…O distance ($D_{O...O}$) of 2.64 Å, and **c** TTF-Bpy-HOF stabilized by O-H…O and O-H…N hydrogen bonds ($D_{O...O}$ = 2.56 Å; $D_{O...N}$ = 2.63 Å) [C (grey), H (white), O (red), N (blue) and S (yellow)].

https://doi.org/10.1038/s41467-025-57939-8

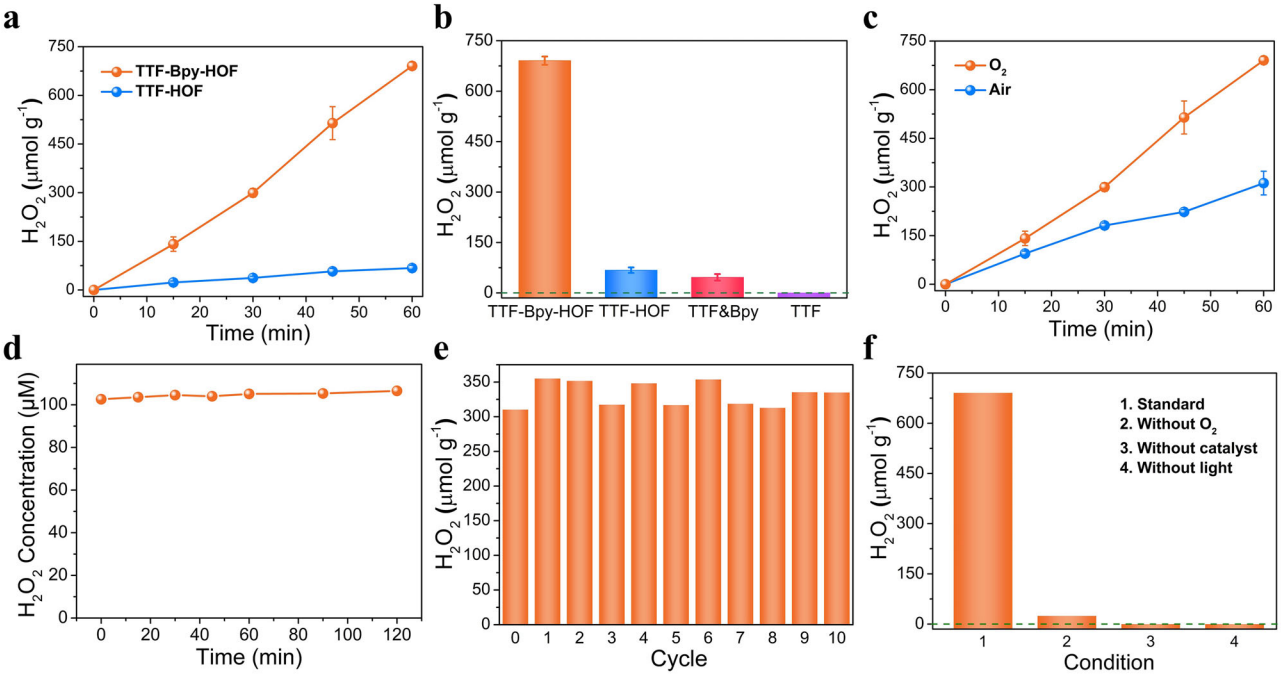

Fig. 2 | Photocatalytic H_2O_2 production activity. a Time-dependent H_2O_2 photogeneration by TTF-HOF and TTF-Bpy-HOF, respectively, in O_2-saturated aqueous solution; **b** photocatalytic activity of TTF-Bpy-HOF, TTF-HOF, TTF&Bpy and TTF for H_2O_2 photosynthesis; **c** time-dependent H_2O_2 photogeneration by TTF-Bpy-HOF in O_2 and air-saturated aqueous solution, respectively (The error bars in **a**–**c** were calculated from the results of three parallel experiments); **d** H_2O_2 (100 μM) degradation study by TTF-Bpy-HOF upon illumination; **e** cycle experiments of TTF-Bpy-HOF for H_2O_2 photosynthesis (reaction time of 30 min for each cycle); **f** control experiments of TTF-Bpy-HOF for H_2O_2 photosynthesis.

The Brunauer-Emmett-Teller (BET) surface areas for TTF-HOF and TTF-Bpy-HOF were determined to be 69.19 $m^2 g^{-1}$ and 52.71 $m^2 g^{-1}$ by the CO_2 sorption experiment at 196 K (Supplementary Fig. 7). Moreover, compared with the FTIR spectrum of TTF-HOF, new absorption peaks at ~810 cm^{-1} were found for TTF-Bpy-HOF, corresponding to the stretch/bending vibration of C-N-C bonds of Bpy (Supplementary Fig. 8)[58]. In addition, XPS analysis and energy-dispersive X-ray spectroscopy (EDS) mappings show the prominent dispersion of N element in TTF-Bpy-HOF, whereas it is absent in TTF-HOF (Supplementary Figs. 9–12). These results show the differences in the compositions of TTF-HOF and TTF-Bpy-HOF, which is consistent with the crystal structures.

The UV–visible diffuse reflection spectrum (UV–vis DRS) for TTF-Bpy-HOF exhibits a strong absorption in the visible range (Supplementary Fig. 13). Compared with TTF-HOF, a broadened light absorption is observed in TTF-Bpy-HOF, which is beneficial for enhancing the solar-to-chemical energy conversion efficiency. The energy gaps derived from the Tauc plots from UV–vis DRS are 1.75 and 1.67 V for TTF-HOF and TTF-Bpy-HOF, respectively (Supplementary Figs. 14 and 15). To determine the energy levels, electrochemical Mott–Schottky (M–S) measurements were carried out (Supplementary Figs. 16 and 17). On the basis of these results, the LUMO positions of TTF-HOF and TTF-Bpy-HOF were calculated to be 0.06 and 0.13 V (*vs.* NHE, pH = 7), respectively, and the HOMO positions of TTF-HOF and TTF-Bpy-HOF were calculated to be 1.81 and 1.80 V (*vs.* NHE, pH = 7), respectively. On the basis of these results, the energy levels of TTF-HOF and TTF-Bpy-HOF can be deduced (Supplementary Fig. 18), which indicates that it is thermodynamically feasible for both HOFs to produce H_2O_2 via O_2 reduction ($E(O_2/H_2O_2)$ = +0.28 V *vs.* NHE, pH = 7) and H_2O oxidation ($E(H_2O_2/H_2O)$ = +1.38 V *vs.* NHE, pH = 7) simultaneously[59,60]. To sum up, TTF-HOF and TTF-Bpy-HOF can theoretically serve as photocatalysts for overall photosynthesis of H_2O_2 by virtue of their suitable energy level structures.

Photocatalytic H_2O_2 production

The experiments of visible-light-driven synthesis of H_2O_2 were conducted in pure water and O_2 atmosphere without any additional co-catalysts, photosensitizers, and sacrificial agents. The H_2O_2 generated was determined by iodometry colorimetry (Supplementary Fig. 19). As shown in Fig. 2a, the kinetic profiles show that the amount of H_2O_2 increases gradually with the illumination time prolonging. The TTF-HOF exhibits a moderate H_2O_2 production rate of 74.4 μmol $g^{-1} h^{-1}$. With the Bpy units introduced, the photocatalytic H_2O_2 production rate of TTF-Bpy-HOF was significantly improved to 681.2 μmol $g^{-1} h^{-1}$, over 9 times higher than that of TTF-HOF (Fig. 2b). Hence, the Bpy units play a significant role in boosting the activity for H_2O_2 photosynthesis. Even under the conditions of pure water and air atmosphere, TTF-Bpy-HOF also shows excellent catalytic performance for H_2O_2 photosynthesis, with a production rate of 271.1 μmol $g^{-1} h^{-1}$ (Fig. 2c and Supplementary Fig. 20). The catalytic performance of TTF-Bpy-HOF is higher than most reported photocatalysts based on MOFs, COFs, graphitic carbon nitride and organic polymers under similar conditions (Supplementary Table 2).

The apparent quantum yields (AQYs) of TTF-Bpy-HOF for photocatalytic H_2O_2 production were further investigated at 450, 470, and 530 nm (Supplementary Fig. 21). It was found that the AQYs of TTF-Bpy-HOF reach as high as 0.34%, 0.30%, and 0.28%, respectively. The different doses of TTF-Bpy-HOF were used for the photosynthesis of H_2O_2. It was found that the production of H_2O_2 increased as the dose of TTF-Bpy-HOF increased (Supplementary Fig. 22a), and the production rate slightly decreased (Supplementary Fig. 22b), probably because the higher catalyst concentration hinders the light absorption and utilization[50]. In addition, the photocatalytic activity of TTF-Bpy-HOF in catalytic systems with different pH values were investigated. The results show that the photocatalytic activity of TTF-Bpy-HOF in acidic solutions is better than in alkaline media (Supplementary Fig. 23), which can be contributed to the $\cdot O_2^-$ species being stabilized under low

https://doi.org/10.1038/s41467-025-57939-8

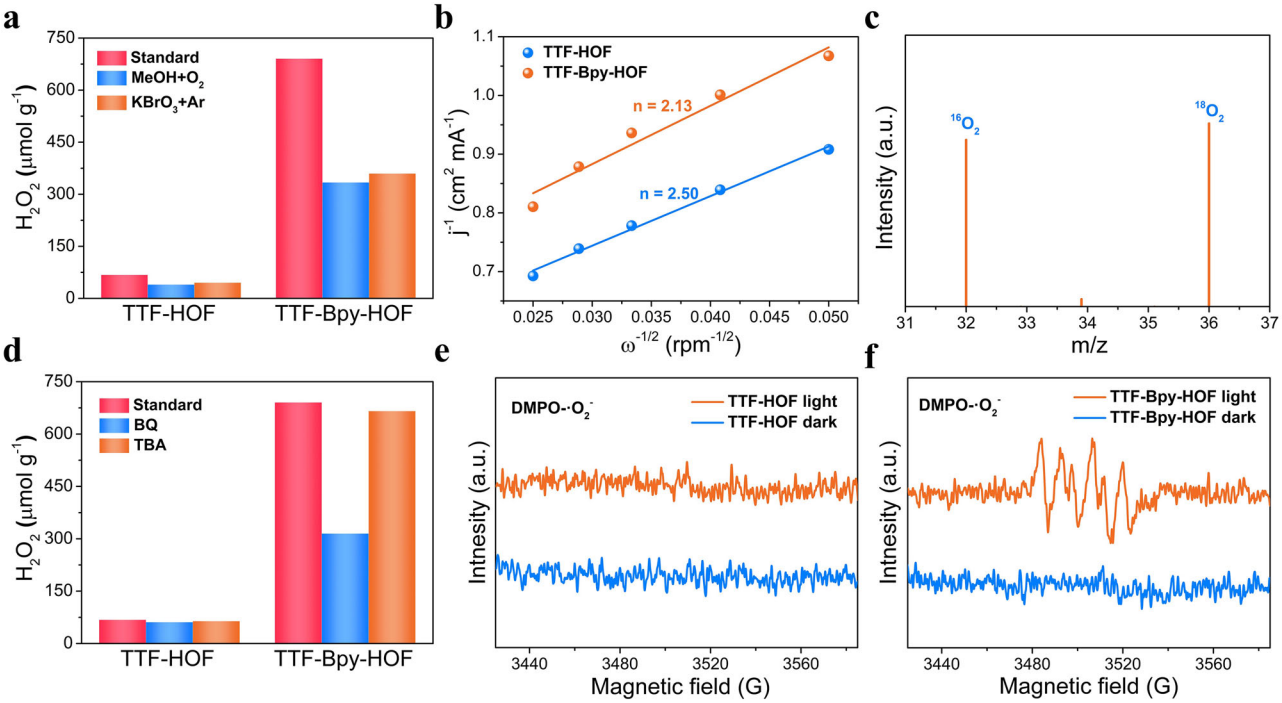

Fig. 3 | Photocatalytic H_2O_2 production activity. a Photocatalytic H_2O_2 generation by TTF-HOF and TTF-Bpy-HOF in $KBrO_4$ (0.5 mM, as the electron acceptor) solution and in CH_3OH (4% *v*/*v*, as the hole acceptor) solution; **b** the Koutecky-Levich plots obtained via RDE measurements in phosphate buffer solution (pH = 7) with continuous O_2 purging; **c** GC-MS of the decomposed products of H_2O_2 generated from photosynthesis by TTF-Bpy-HOF in $^{16}O_2$-saturated $H_2{}^{18}O$ solution; **d** the contribution of different active species in H_2O_2 photosynthesis by TTF-HOF and TTF-Bpy-HOF (BQ: p-benzoquinone, TBA: tert-butanol); EPR spectra of DMPO-$\cdot O_2^-$ of **e** TTF-HOF and **f** TTF-Bpy-HOF.

pH conditions to accelerate the formation of H_2O_2[61]. It was found that as the pH value decreased, the photocatalytic activity of TTF-Bpy-HOF for H_2O_2 production first increased (Supplementary Fig. 24), reaching a maximum of 938 μmol g^{-1} h^{-1} at pH = 5; however, when the pH value further decreased to 3, the photocatalytic activity of TTF-Bpy-HOF dropped sharply, which can be attributed to the instability of TTF-Bpy-HOF under strong acidic conditions, as confirmed by the powder XRD results (Supplementary Fig. 25).

To prove the contribution of hydrogen bonds in TTF-HOF and TTF-Bpy-HOF for the photosynthesis of H_2O_2, we further evaluated the performances of TTF and the physical mixture of TTF and Bpy (TTF&Bpy) (Fig. 2b). The results show that under the same condition, almost no H_2O_2 was generated over TTF, and only a limited amount of H_2O_2 was detected when TTF&Bpy was used as the photocatalyst (Fig. 2b and Supplementary Fig. 26). These results verify that the hydrogen-bond-mediated ordered structures of TTF-HOF and TTF-Bpy-HOF are important to their catalytic activity in H_2O_2 photosynthesis. Their long-range ordered structures may provide special electron transfer channels, which can accelerate the electron transfer rate and boost the photocatalytic H_2O_2 production. The possible decomposition of H_2O_2 over TTF-HOF and TTF-Bpy-HOF under light irradiation was investigated. As depicted in Fig. 2d and Supplementary Fig. 27, the concentrations of H_2O_2 barely changed under continuous irradiation for 2 h, implying that the H_2O_2 is stable in the presence of TTF-HOF/TTF-Bpy-HOF and light irradiation. Besides, TTF-Bpy-HOF exhibits a good stability during the process of H_2O_2 photosynthesis. For 10 catalytic cycles, the amounts of generated H_2O_2 were almost identical (Fig. 2e), indicating that TTF-Bpy-HOF can serve as a stable photocatalyst for H_2O_2 photosynthesis. Besides, the structural integrity of TTF-Bpy-HOF was also confirmed via XRD, FTIR, and SEM measurements (Supplementary Figs. 28–30). The powder XRD data showed that TTF-HOF can also keep stable after the photocatalytic reaction (Supplementary Fig. 31).

To investigate the reaction process of H_2O_2 generation in further depth, a series of control experiments of H_2O_2 photosynthesis over TTF-Bpy-HOF were carried out. As illustrated in Fig. 2f, no H_2O_2 was generated in the absence of TTF-Bpy-HOF or illumination, suggesting that both photocatalyst and light are indispensable. When O_2 was replaced by Ar, H_2O_2 could barely be detected, suggesting that the O_2 reduction reaction was indeed involved in H_2O_2 photosynthesis[62]. To further confirm the origin of H_2O_2, the photocatalytic O_2 reduction over TTF-HOF and TTF-Bpy-HOF were performed in the presence of methanol (as the sacrificial agent to replace H_2O)[16]. As shown in Fig. 3a, an appreciable amount of H_2O_2 can be observed, which is attributed to the O_2 reduction by photogenerated electrons. On the other hand, the photocatalytic H_2O oxidation over TTF-HOF and TTF-Bpy-HOF were also carried out using $KBrO_3$ as an electron scavenger in an Ar-saturated aqueous solution. A considerable amount of H_2O_2 was detected, indicating that the H_2O was photocatalytically oxidized to H_2O_2.

We further examined the process of H_2O_2 photosynthesis by rotating disk electrode (RDE) and rotating ring-disk electrode (RRDE) measurements. As shown in Fig. 3b, on the basis of linear sweep voltammetry (LSV) curves obtained from RDE, the average electron transfer numbers (*n*) of O_2 reduction, excavated from Koutecky–Levich (K–L) plots, were 2.5 and 2.13 on TTF-HOF and TTF-Bpy-HOF, respectively (Fig. 3b and Supplementary Fig. 32), which confirms that $2e^-$ O_2 reduction process has occurred. The *n* value for TTF-Bpy-HOF is closer to 2 than that of TTF-HOF, demonstrating that the selectivity for $2e^-$ O_2 reduction is improved after the introduction of Bpy units[63]. On the other side, to elucidate the $2e^-$ H_2O oxidation process, RRDE tests were conducted under Ar conditions. The potential of the rotating disk electrode was scanned from 0.2 to 2.5 V (vs Ag/AgCl) with a scan rate of 10 mV s^{-1}, while a constant potential of −0.23 V was maintained on the Pt ring electrode[64,65]. Herein, if O_2 was produced in the $4e^-$ H_2O oxidation by rotating the disc electrode, it would quickly

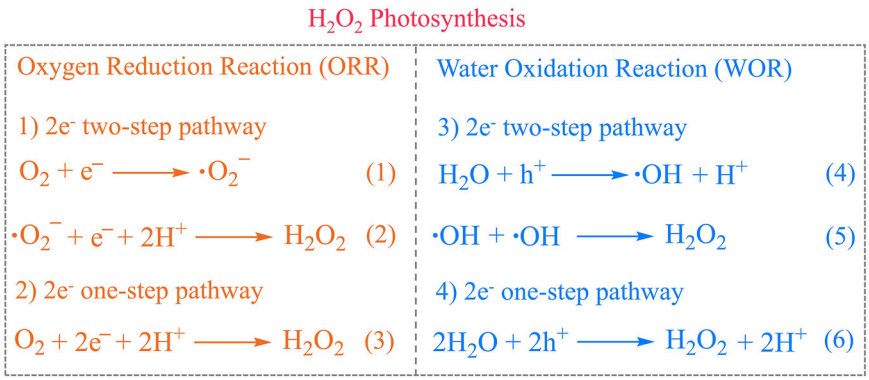

Fig. 4 | The pathways of H_2O_2 photosynthesis. The pathways of H_2O_2 photosynthesis via oxygen reduction reaction and water oxidation reaction.

diffuse to the ring electrode and be reduced, yielding a discernible detection signal[25]. As shown in Supplementary Fig. 33, the disk currents escalated with potentials higher than 1.5 V (vs Ag/AgCl), indicating that H_2O oxidation occurred at the rotating disk electrode for TTF-Bpy-HOF. No reduction currents were observed at the Pt ring electrode for TTF-Bpy-HOF, implying the inability to generate O_2 via H_2O oxidation. However, when the potential applied to the ring electrode was changed to +0.6 V (vs Ag/AgCl), oxidation current changes existed, which can be attributed to the oxidation of H_2O_2 on the Pt ring electrode. This result revealed that the $2e^-$ H_2O oxidation route occurs over TTF-Bpy-HOF for H_2O_2 production[25,64]. Similar results can be observed on TTF-HOF as well (Supplementary Fig. 34).

The ^{18}O isotopic labeling experiments were further conducted to confirm the origin of the generated H_2O_2. The produced H_2O_2 was detected by gas chromatography-mass spectrometry via converting it to O_2 with the assistance of MnO_2. The experiment of H_2O_2 photosynthesis over TTF-Bpy-HOF was investigated in $^{16}O_2$-saturated $H_2{}^{18}O$ solution. The ratio of $^{18}O_2$ and $^{16}O_2$ derived from the decomposition of photogenerated H_2O_2 is close to 1:1 (Fig. 3c), which is consistent with the theoretical value. The above results solidly evidence that the H_2O_2 photosynthesis over TTF-HOF and TTF-Bpy-HOF undergoes the dual channels of $2e^-$ O_2 reduction and $2e^-$ H_2O oxidation.

Catalytic mechanism

It is well known that the routes of H_2O_2 photosynthesis via O_2 reduction include a $2e^-$ two-step process with $\cdot O_2^-$ as the intermediate species [Fig. 4, Eqs. (1)-(2)], and a $2e^-$ one-step process [Fig. 4, Eq. (3)][66]. The routes of H_2O_2 photosynthesis via H_2O oxidation include a $2e^-$ two-step process with ·OH as the intermediate species [Fig. 4, Eqs. (4)-(5)], and a $2e^-$ one-step process [Fig. 4, Eq. (6)][66]. To clarify the reaction pathways of O_2 reduction and H_2O oxidation for H_2O_2 photosynthesis over TTF-HOF and TTF-Bpy-HOF, the quenching tests of the active species were performed, in which p-benzoquinone (BQ) and tert-butanol (TBA) were employed as the scavengers for $\cdot O_2^-$ and ·OH radicals, respectively[67]. As shown in Fig. 3d, the photocatalytic H_2O_2 production over TTF-HOF and TTF-Bpy-HOF did not decline when TBA was added to the reaction system, which indicates that for both TTF-HOF and TTF-Bpy-HOF, the H_2O oxidation goes through a $2e^-$ one-step process to synthesize H_2O_2. On the other hand, the photocatalytic H_2O_2 production over TTF-HOF was almost unaffected when BQ was added, whereas TTF-Bpy-HOF was significantly inhibited after BQ addition. These observations indicate that for TTF-HOF, the H_2O_2 photocatalysis via O_2 reduction undergoes a $2e^-$ one-step process, whereas for TTF-Bpy-HOF, it undergoes a $2e^-$ two-step process, where $\cdot O_2^-$ is the detected important intermediate.

The electron paramagnetic resonance (EPR) measurements were further performed to detect the active oxygen species possibly generated during the H_2O_2 photosynthesis; 5,5-diemthyl-1-pyrroline *N*-oxide (DMPO) was used as the spin-trap agent. The EPR spectra for TTF-HOF and TTF-Bpy-HOF show that no signal of DMPO-·OH was detected during the photocatalytic processes (Supplementary Fig. 35). Of note, no signal of DMPO-$\cdot O_2^-$ was detected for TTF-HOF, whereas a typical six characteristic signals of DMPO-$\cdot O_2^-$ was clearly observed for TTF-Bpy-HOF (Fig. 3e, f), which indicates the formation of $\cdot O_2^-$ intermediates. These observations further confirm that the H_2O oxidation over both TTF-HOF and TTF-Bpy-HOF undergoes $2e^-$ one-step processes, while the O_2 reduction over TTF-HOF and TTF-Bpy-HOF goes through different reaction routes. The former is a $2e^-$ one-step process, whereas the latter is a $2e^-$ two-step process. This result is consistent with the results of the above quenching tests[68]. Furthermore, the in situ FTIR spectra for TTF-HOF and TTF-Bpy-HOF were recorded during the processes of H_2O_2 photosynthesis. As shown in Supplementary Fig. 36, for TTF-HOF, the peak intensity at 1384 cm^{-1} gradually increased with the proceeding of the photocatalytic reaction, which can be assigned to the surface-adsorbed hydroperoxide (HOOH*)[69]. Notably, compared with TTF-HOF, two new vibration peaks located at 1200 and 1220 cm^{-1} were observed for TTF-Bpy-HOF, which can be assigned to ·OOH* and $\cdot O_2^-$*, respectively[25,69]. $\cdot O_2^-$ is the single-electron reduction product of O_2, which indicates that the O_2 photoreduction over TTF-Bpy-HOF undergoes the $2e^-$ two-steps process to produce H_2O_2.

To understand the greatly enhanced photocatalytic activity of TTF-Bpy-HOF in H_2O_2 photosynthesis, photoluminescence (PL) spectroscopy was performed. Clearly, the PL spectra for TTF-Bpy-HOF show significantly damped emission compared with that for TTF-HOF, suggesting the greatly suppressed recombination of the photogenerated electrons and holes (Fig. 5a). Moreover, the time-resolved photoluminescence (TRPL) spectra revealed a shortened average exciton lifetime of 2.03 ns for TTF-HOF with respect to 0.82 ns for TTF-Bpy-HOF, illustrating that the introduction of Bpy units significantly accelerates the charge transfer (Fig. 5b). The photocurrent response test showed that the TTF-Bpy-HOF has a higher photocurrent density than TTF-HOF, indicating the better separation efficiency of photo-induced electrons in TTF-Bpy-HOF than in TTF-HOF (Fig. 5c). To gain more insights into the charge transfer kinetics, the electrochemical impedance spectroscopy (EIS) was further carried out on TTF-HOF and TTF-Bpy-HOF. As shown in Fig. 5d, the semicircle arc radius of the Nyquist plot for TTF-Bpy-HOF is significantly smaller than that of TTF-HOF, which also indicates the faster charge transfer in TTF-Bpy-HOF, facilitating the separation efficiency of photogenerated electrons and holes. In addition, the superior performance of TTF-Bpy-HOF was clarified using RDE and RRDE measurements in a 0.1 M phosphate buffer solution (PBS). The LSV curves obtained from RDE show that the initial potential and half-wave potential for TTF-Bpy-HOF is more positive than for TTF-HOF, which indicates the superior O_2 reduction catalytic activity for TTF-Bpy-HOF over TTF-HOF (Fig. 5e). The ring current for TTF-Bpy-HOF is much higher than for TTF-HOF,

https://doi.org/10.1038/s41467-025-57939-8

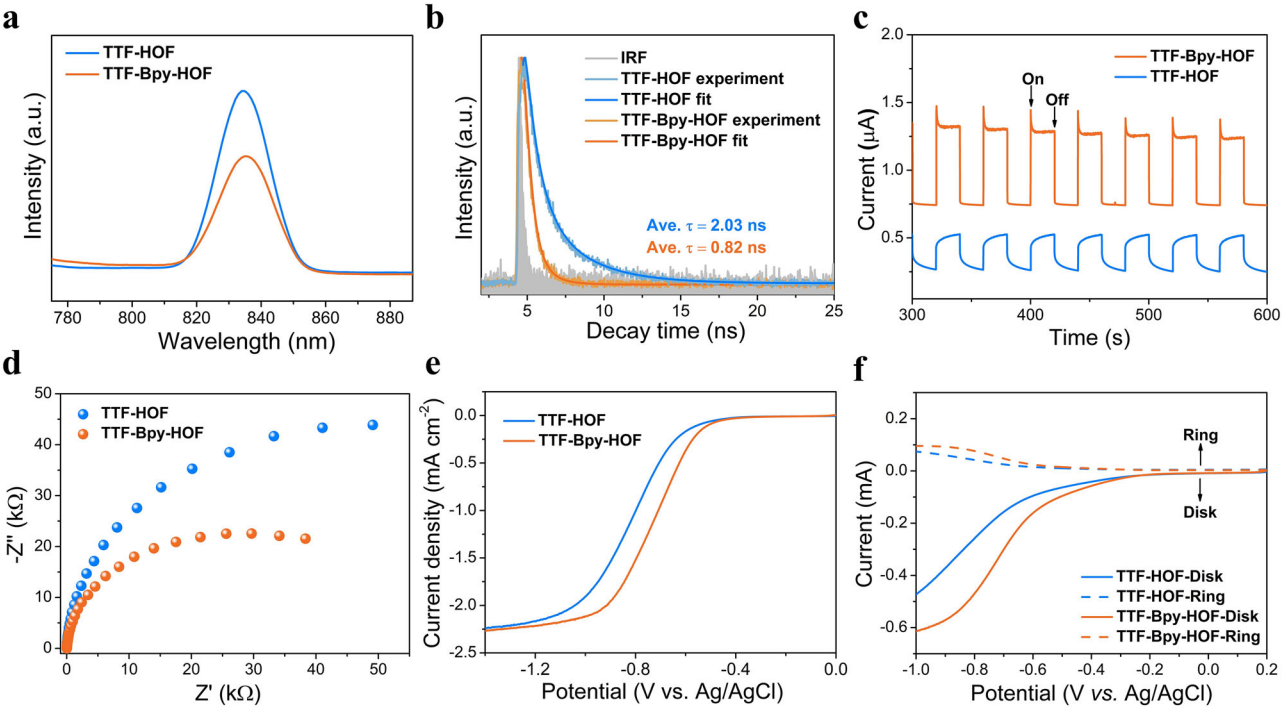

Fig. 5 | Spectroscopic and electrochemical characterization. **a** Photoluminescent spectra, **b** time-resolved photoluminescence spectroscopy, **c** transient photocurrent response and **d** electrochemical impedance spectroscopy of TTF-HOF and TTF-Bpy-HOF (IRF instrument response function); **e** linear-sweep RDE voltammograms and **f** RRDE polarization curve of TTF-HOF and TTF-Bpy-HOF measured at 1600 rpm in 0.1 M phosphate buffer solution under O_2 atmosphere.

demonstrating that more H_2O_2 was produced over TTF-Bpy-HOF (Fig. 5f). Besides, a higher oxidation current for TTF-Bpy-HOF was observed under Ar atmosphere from RRDE measurement, suggesting the enhanced H_2O oxidation performance of TTF-Bpy-HOF over TTF-HOF (Supplementary Fig. 37). Moreover, the hydrophilicity of TTF-HOF and TTF-Bpy-HOF were studied by the water contact angle measurements. TTF-Bpy-HOF was found to be more hydrophobic (with a contact angle of 95°) than TTF-HOF (82°), which was conducive to H_2O_2 desorption, thus promoting the $2e^-$ O_2 reduction reaction (ORR) and $2e^-$ water oxidation reaction (WOR) (Supplementary Fig. 38)[20,68].

To sum up, the above experimental results solidly support the better catalytic activity of TTF-Bpy-HOF than TTF-HOF in the overall photosynthesis of H_2O_2. The introduction of Bpy, by constructing TTF-Bpy donor–acceptor structural units in TTF-Bpy-HOF, well accelerates the electron transfer and effectively inhibits the recombination of the photogenerated electrons and holes, thus greatly boosting the catalytic activity of H_2O_2 overall photosynthesis. It should be noted that the catalytic activities of TTF-Bpy-HOF and TTF-HOF are determined by multiple factors. Despite the fact that the BET surface area of TTF-Bpy-HOF is slightly lower than that of TTF-HOF (Supplementary Fig. 7), the introduction of Bpy provides more active sites and electron transfer channels, which endows TTF-Bpy-HOF with a higher catalytic activity.

The enhanced catalytic activity of TTF-Bpy-HOF in H_2O_2 overall photosynthesis was further elucidated theoretically. As shown in Fig. 6a, the primary contribution to the HOMO and LUMO in TTF-HOF predominantly arises from the TTF part. In contrast, in TTF-Bpy-HOF, the HOMO and LUMO are primarily localized on the TTF and Bpy parts, respectively, which indicates a pronounced spatial separation between these orbitals. This pronounced spatial separation, similar to the concept of reported “spatially separated redox centers”, helps to suppress electron–hole recombination and enhance the photocatalytic efficiency for H_2O_2 production[70]. Furthermore, the excited-state electronic structures of TTF-HOF and TTF-Bpy-HOF were further calculated using the time-dependent density functional theory (TD-DFT) method. The results show that TTF-Bpy-HOF, featuring the donor–acceptor structure, has a better charge separation efficiency (Supplementary Fig. 39)[71], which agrees well with the experiment results. In addition, the charge transfer (Q (e)) for the hydrogen bonds of O–H···O and O–H···N was calculated. As shown in Supplementary Table 3, the O–H···N hydrogen bond exhibited more charge transfer than O–H···O, indicative of more efficient electron transfer of O–H···N than O–H···O, which could also contribute to the enhanced photocatalytic activity of TTF-Bpy-HOF[72,73]. On the basis of the above characterizations and theoretical calculation results, a plausible mechanism of TTF-Bpy-HOF for H_2O_2 overall photosynthesis could be proposed. As shown in Fig. 6b, under visible light illumination, the TTF units in TTF-Bpy-HOF absorb photons and the electron–hole pair separates. The photogenerated electron transfers to the Bpy moiety and the photogenerated hole stays in the TTF moiety. Thereafter, the ORR and WOR occur simultaneously on these two moieties. The water oxidation reaction undergoes a direct $2e^-$ one-step process to photosynthesize H_2O_2 on the TTF unit of TTF-Bpy-HOF, while the O_2 reduction reaction goes through a $2e^-$ two-step process [Fig. 4, Eq. (6)], that is, the N atom of Bpy accepts an electron from TTF upon illumination, and then the electron transfers to the O_2 adsorbed on the N atom to form $\cdot O_2^-$ intermediate [Fig. 4, Eq. (1)], then the $\cdot O_2^-$ intermediate further accepts one electron and two protons to generate H_2O_2 [Fig. 4, Eq. (2)].

Density functional theory (DFT) calculations were performed to probe the catalytic mechanism of TTF-Bpy-HOF for H_2O_2 photosynthesis in further depth (Supplementary Table 4 and Supplementary Figs. 40–45). First, the O_2 adsorption sites in TTF-HOF and TTF-Bpy-HOF were investigated. The results show that the phenyl groups of TTF-HOF have higher adsorption energy (Supplementary Fig. 41), which indicates that O_2 molecule is more easily adsorbed on the phenyl rings in TTF-HOF. After the introduction of Bpy units, however, the O_2 molecule is more likely to adsorb onto the pyridyl rings in the TTF-Bpy-HOF and then O_2 reduction reaction ensues (Supplementary Fig. 42). The reaction pathway and corresponding Gibbs free energy differences (ΔG) of O_2 reduction and H_2O oxidation over TTF-HOF and TTF-

https://doi.org/10.1038/s41467-025-57939-8

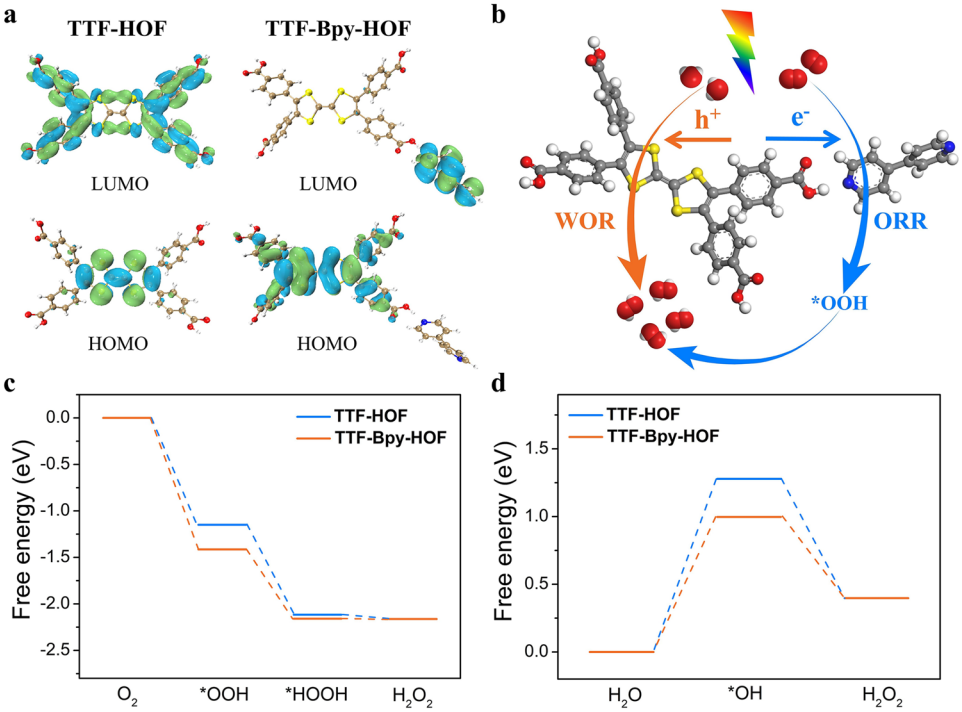

Fig. 6 | DFT calculation. a HOMO and LUMO of TTF-HOF and TTF-Bpy-HOF; **b** schematic diagram of the photosynthesized H_2O_2 through the O_2 reduction reaction (ORR) and water oxidation reaction (WOR) pathways; calculated free-energy diagrams of **c** O_2 reduction and **d** water oxidation pathways toward H_2O_2 production on the TTF-HOF and TTF-Bpy-HOF.

Bpy-HOF were further studied by DFT calculations (Supplementary Figs. 43–45). As shown in Fig. 6c, the entire processes of O_2 reduction to H_2O_2 are spontaneous with the energy diagram going downhill for both TTF-HOF and TTF-Bpy-HOF. Notably, the ΔG value for the formation of *OOH was −1.415 eV for TTF-Bpy-HOF, which is lower than that for TTF-HOF (−1.149 eV), suggesting that the adsorbed O_2 on the TTF-Bpy-HOF could be more easily activated into *OOH, which then undergoes further protonation to form *HOOH. Additionally, H_2O_2 easily desorbs from TTF-Bpy-HOF on account of its downhill energy landscape, thereby leading to more efficient H_2O_2 generation. For H_2O oxidation to generate H_2O_2, the formation processes of *OH intermediates are non-spontaneous, and the step of two *OH intermediates further combining to form H_2O_2 is spontaneous (Fig. 6d). Thus, *OH formation is the rate-determining step (RDS) here. Notably, the ΔG of RDS for TTF-Bpy-HOF (0.997 eV) is much lower than for TTF-HOF (1.278 eV), indicating that the activity of TTF-Bpy-HOF for H_2O_2 production is much better than that of TTF-HOF, which is in consistency with the experimental observations.

Discussion

In summary, we have found that constructing donor–acceptor HOFs can greatly enhance the photocatalytic activity for overall photosynthesis of H_2O_2 from H_2O and O_2. In the absence of any additional co-catalysts, photosensitizers, and sacrificial agents, the donor–acceptor TTF-Bpy-HOF can couple the O_2 reduction reaction with water oxidation reaction, simultaneously producing H_2O_2 under visible light illumination. The production rate reaches as high as 681.2 μmol g^{-1} h^{-1}, over 9 times higher than for TTF-HOF. The results of experiments and DFT calculation reveal that the introduced Bpy units in TTF-Bpy-HOF not only optimize the reaction paths but also promote the charge separation and optimize electron transfer, thus greatly boosting the catalytic performance for overall H_2O_2 photosynthesis. This work paves the way for the rational design of efficient HOFs-based catalysts for artificial photosynthesis.

Methods

Materials and characterization

Tetrahydrofuran (AR, Energy Chemicals), 4,4′-Bipyridine (98%, Energy Chemicals), Tetrathiafulvalene-3,4,5,6-tetrakis(4-benzoicacid) (98%, Adamas-beta), Potassium hydrogen phthalate ($C_8H_5KO_4$, 99%, Aladdin), potassium iodide (KI, 99%, Aladdin). All chemicals and materials were commercially obtained and used without further purification. Solvents were dried and distilled before being used for catalyst synthesis. The purity of N_2, Ar and O_2 are 99.999%. Powder XRD patterns were collected on a smart X-ray diffractometer (SmartLab 9 kW, Rigaku, Japan) equipped with Cu Kα radiation (λ = 1.54178 Å). FT-IR and in situ FT-IR spectra were recorded on Nicolet iS50 IR spectrometers, and samples were tableted with KBr as support. SEM images were acquired on a Zeiss Supra 40 field emission scanning electron microanalyzer. UV-Vis absorption spectra were recorded on a U-3900 UV/VIS spectrophotometer (Hitachi). Steady-state photoluminescence (PL) spectra were measured using a F-4600 Fluorescence spectrophotometer (Hitachi). Time-resolved photoluminescence decays were detected with a FLS-1000 steady state and transient state fluorescence spectrometer (Edinburgh Instruments Ltd.). X-ray photoelectron spectroscopy (XPS) measurements were carried out on an ESCALAB250Xi X-ray photoelectron spectrometer with Al Kα as the excitation source (Thermo Scientific). Electron paramagnetic resonance (EPR) spectra were measured on EMXplus-6/1 (Bruker, Germany). The isotope of ^{18}O for O_2 was analyzed using mass spectrometry (HPR-20 QIC).

Synthesis of TTF-HOF

TTF-HOF was synthesized according to the literature method[55]. Tetrathiafulvalene tetracarboxylic acid (TTF; 30 mg, 0.044 mmol) was dissolved in 10 mL water and THF (v/v = 1:1) solution, and the mixed solution was transformed into a 20 mL vial. Then the vial was placed in an oven at 60 °C for 72 h without screwing on the cap to allow the THF to evaporate gradually. After cooling to room temperature, dark brownish-red crystals were obtained (25.8 mg, 86% yield).

Synthesis of TTF-Bpy-HOF

TTF-Bpy-HOF was synthesized according to the literature method[56]. TTF (9.8 mg, 0.015 mmol) and 4,4′-bipyridine (Bpy; 4.7 mg, 0.03 mmol) were dissolved in THF (10 ml), the mixture was stirred at 55 °C for 2 h, filtered and slowly evaporated, black crystals formed from the solution (4.1 mg, 28% yield based on TTF).

Photocatalytic H_2O_2 production

In a typical experiment, the photosynthesis of H_2O_2 was carried out in a 18 mL glass tube containing 1 mg photocatalyst and 5 mL deionized water at 25 °C under O_2 atmosphere. Then, the system was irradiated by a 300 W Xe lamp (Microsolar300, Beijing Perfectlight) with a 420 nm cutoff filter.

Photoelectrochemical measurements

The photoelectrochemical properties of TTF-HOF and TTF-Bpy-HOF were carried out on an electrochemical workstation (CHI760E) with a standard three-electrode photoelectron chemical cell by a modified literature method. The prepared fluoride tin oxide (FTO) coated with samples, platinum wire, and Ag/AgCl act as the working, auxiliary and reference electrode, respectively[74]. The working electrode FTO coated with HOF materials was prepared as follows. Firstly, the pristine FTO electrode was cleaned by ultrasonication in distilled water, absolute ethanol, acetone and absolute ethanol for 20 min sequentially, and dried in vacuum. Then HOF materials (2 mg) dispersed in a mixed solution of deionized water (990 μL) and Nafion (10 μL) was ultrasonicated for 2 h, and ground to obtain slurry, which was uniformly coated onto the 1 cm × 2 cm treated FTO electrode. The coated FTO electrode was dried at room temperature over night to obtain the working electrode. The photocurrent was measured at 0.2 V (vs. Ag/AgCl) with a 300 W Xe lamp by intermittent irradiation. Mott-Schottky plots were obtained under direct current potential polarization at different frequencies of 800, 1000, and 1200 Hz, respectively. The electrochemical impedance spectra (EIS) were recorded at an applied potential of −0.4 V versus Ag/AgCl over the frequency range of 1 MHz to 0.1 Hz. All the photoelectrochemical measurements were performed in 0.5 M Na_2SO_4 (pH = 6.8) electrolytes bubbled with N_2 for 30 min before test.

Computational details

Quantum chemical studies were performed using density functional theory (DFT) implemented in the GAUSSIAN 16 package. Geometry optimization and frequency analysis were calculated at B3LYP hybrid functional with GD3BJ correction under the level of 6-311 G(D) basis sets. The adsorption energy of the different molecular fragments representing the HOFs is calculated as follows: $Eads(A) = E(*A) - E(*) - E(A)$. Gibbs free energies ($G$) of the molecules are also performed at the level of B3LYP-D3BJ/6-311 G(D).

Statistics and reproducibility

The experiments were not randomized.

Data availability

The data that support the findings of this study are available within the paper and Supplementary Information files. Source data are provided with this paper.

References

1. Perry, S. C. et al. Electrochemical synthesis of hydrogen peroxide from water and oxygen. *Nat. Rev. Chem.* **3**, 442–458 (2019).
2. Xia, C., Kim, J. Y. & Wang, H. T. Recommended practice to report selectivity in electrochemical synthesis of H_2O_2. *Nat. Catal.* **3**, 605–607 (2020).
3. Sun, Y. Y., Han, L. & Strasser, P. A comparative perspective of electrochemical and photochemical approaches for catalytic H_2O_2 production. *Chem. Soc. Rev.* **49**, 6605–6631 (2020).
4. Chen, L. et al. Acetylene and diacetylene functionalized covalent triazine frameworks as metal-free photocatalysts for hydrogen peroxide production: a new two-electron water oxidation pathway. *Adv. Mater.* **32**, 1904433 (2020).
5. Tan, D. et al. Covalent organic frameworks enable sustainable solar to hydrogen peroxide. *Adv. Funct. Mater.* **34**, 2311655 (2024).
6. He, T. & Zhao, Y. L. Covalent organic frameworks for efficient hydrogen peroxide production. *EnergyChem* **6**, 100121 (2024).
7. Shiraishi, Y. et al. Resorcinol-formaldehyde resins as metal-free semiconductor photocatalysts for solar-to-hydrogen peroxide energy conversion. *Nat. Mater.* **18**, 985–993 (2019).
8. Zhang, Y., Pan, C., Li, J. & Zhu, Y. Recent progress in nonsacrificial H_2O_2 generation using organic photocatalysts and in situ applications for environmental remediation. *Acc. Mater. Res.* **5**, 76–88 (2024).
9. Hou, H. L., Zeng, X. K. & Zhang, X. W. Production of hydrogen peroxide by photocatalytic processes. *Angew. Chem. Int. Ed.* **59**, 17356–17376 (2020).
10. Wu, S., Yu, H. T., Chen, S. & Quan, X. Enhanced photocatalytic H_2O_2 production over carbon nitride by doping and defect engineering. *ACS Catal.* **10**, 14380–14389 (2020).
11. Sun, P. Z., Tyree, C. & Huang, C.-H. Inactivation of escherichia coli, bacteriophage MS2, and bacillus spores under UV/H_2O_2 and UV/peroxydisulfate advanced disinfection conditions. *Environ. Sci. Technol.* **50**, 4448–4458 (2016).
12. Zeng, X. K., Liu, Y., Hu, X. Y. & Zhang, X. W. Photoredox catalysis over semiconductors for light-driven hydrogen peroxide production. *Green Chem.* **23**, 1466–1494 (2021).
13. Feng, S. F. et al. Rational design of covalent organic frameworks with redox-active catechol moieties for high-performance overall photosynthesis of hydrogen peroxide. *ACS Catal.* **14**, 7736–7745 (2024).
14. Yu, W. Y. et al. Photocatalytic hydrogen peroxide evolution: what is the most effective strategy? *Nano Energy* **104**, 107906 (2022).
15. Li, K. J. et al. Highly efficient photocatalytic H_2O_2 production in microdroplets: accelerated charge separation and transfer at interfaces. *Energy Environ. Sci.* **16**, 1135–1145 (2023).
16. Teng, Z. Y. et al. Atomically dispersed antimony on carbon nitride for the artificial photosynthesis of hydrogen peroxide. *Nat. Catal.* **4**, 374–384 (2021).
17. Wei, Z. et al. Efficient visible-light-driven selective oxygen reduction to hydrogen peroxide by oxygen-enriched graphitic carbon nitride polymers. *Energy Environ. Sci.* **11**, 2581–2589 (2018).
18. Zhang, J.-H. et al. Metal-organic layers as a platform for developing single-atom catalysts for photochemical CO_2 reduction. *Nano Energy* **80**, 105542 (2021).
19. Qiu, J. H., Dai, D. L. & Yao, J. F. Tailoring metal-organic frameworks for photocatalytic H_2O_2 production. *Coord. Chem. Rev.* **501**, 215597 (2024).
20. Isaka, Y., Kawase, Y. D., Kuwahara, Y. & Mori, K. Two-phase system utilizing hydrophobic metal-organic frameworks (MOFs) for photocatalytic synthesis of hydrogen peroxide. *Angew. Chem. Int. Ed.* **58**, 5402–5406 (2019).
21. Yong, Z. J. & Ma, T. Y. Solar-to-H_2O_2 catalyzed by covalent organic frameworks. *Angew. Chem. Int. Ed.* **62**, e202308980 (2023).
22. Zhi, Q. J. et al. Piperazine-linked metal phthalocyanine frameworks for highly efficient visible-light-driven H_2O_2 photosynthesis. *J. Am. Chem. Soc.* **144**, 21328–21336 (2022).
23. Li, L. Y. et al. Custom-design of strong electron/proton extractor on COFs for efficient photocatalytic H_2O_2 production. *Angew. Chem. Int. Ed.* **63**, e202320218 (2024).
24. Zhao, W. et al. Accelerated synthesis and discovery of covalent organic framework photocatalysts for hydrogen peroxide production. *J. Am. Chem. Soc.* **144**, 9902–9909 (2022).

25. Chang, J.-N. et al. Oxidation-reduction molecular junction covalent organic frameworks for full reaction photosynthesis of H_2O_2. *Angew. Chem. Int. Ed.* **62**, e202218868 (2024).
26. Kim, H., Shim, K., Lee, K. E., Han, J. W. & Zhu, Y. F. Photocatalytic production of H_2O_2 from water and dioxygen only under visible light using organic polymers: systematic study of the effects of heteroatoms. *Appl. Catal. B Environ. Energy* **299**, 120666 (2021).
27. Xie, Z. et al. Variation of chemical microenvironment of pores in hydrazone-linked covalent organic frameworks for photosynthesis of H_2O_2. *Angew. Chem. Int. Ed.* **63**, e202410179 (2024).
28. Liu, L. et al. Linear conjugated polymers for solar-driven hydrogen peroxide production: the importance of catalyst stability. *J. Am. Chem. Soc.* **143**, 19287–19293 (2021).
29. Baek, J. H. et al. Selective and efficient Gd-Doped $BiVO_4$ photoanode for two-electron water oxidation to H_2O_2. *ACS Energy Lett.* **4**, 720–728 (2019).
30. Wang, B., Lin, R.-B., Zhang, Z., Xiang, S. C. & Chen, B. L. Hydrogen-bonded organic frameworks as a tunable platform for functional materials. *J. Am. Chem. Soc.* **142**, 14399–14416 (2020).
31. Lin, R.-B. et al. Multifunctional porous hydrogen-bonded organic framework materials. *Chem. Soc. Rev.* **48**, 1362–1389 (2019).
32. Zhang, Z., Ye, Y., Xiang, S. C. & Chen, B. L. Exploring multifunctional hydrogen-bonded organic framework materials. *Acc. Chem. Res.* **55**, 3752–3766 (2022).
33. Hu, F. et al. An ultrastable and easily regenerated hydrogen-bonded organic molecular framework with permanent porosity. *Angew. Chem. Int. Ed.* **56**, 2101–2104 (2017).
34. Hisaki, I. et al. Acid responsive hydrogen-bonded organic frameworks. *J. Am. Chem. Soc.* **141**, 2111–2121 (2019).
35. Wang, Y., Song, L.-N., Wang, X.-X., Wang, Y.-F. & Xu, J.-J. Hydrogen-bonded organic frameworks-based electrolytes with controllable hydrogen bonding networks for solid-state lithium batteries. *Angew. Chem. Int. Ed.* **63**, e202401910 (2024).
36. Ma, K. K. et al. Ultrastable mesoporous hydrogen-bonded organic framework-based fiber composites toward mustard gas detoxification. *Cell Rep. Phys. Sci.* **1**, 100024 (2020).
37. Hisaki, I. et al. Hexaazatriphenylene-based hydrogen-bonded organic framework with permanent porosity and single-crystallinity. *Chem. Eur. J.* **23**, 11611–11619 (2017).
38. Li, Y. T. et al. Hydrogen-bonded frameworks for molecular structure determination. *Nat. Commun.* **10**, 4477 (2019).
39. Liang, W. B. et al. Enzyme encapsulation in a porous hydrogen-bonded organic framework. *J. Am. Chem. Soc.* **141**, 14298–14305 (2019).
40. Luo, X.-Z. et al. A microporous hydrogen-bonded organic framework: exceptional stability and highly selective adsorption of gas and liquid. *J. Am. Chem. Soc.* **135**, 11684–11687 (2013).
41. Zhang, J.-H. et al. Ordered heterogeneity of molecular photosensitizer toward enhanced photocatalysis. *Proc. Natl Acad. Sci. USA* **119**, e2118278119 (2022).
42. Yin, Q. et al. An ultra-robust and crystalline redeemable hydrogen-bonded organic framework for synergistic chemo-photodynamic therapy. *Angew. Chem. Int. Ed.* **57**, 7691–7696 (2018).
43. Chen, G., Huang, S., Ma, X., He, R. & Ouyang, G. F. Encapsulating and stabilizing enzymes using hydrogen-bonded organic frameworks. *Nat. Protoc.* **18**, 2032–2050 (2023).
44. Chen, S. M. et al. Photo responsive electron and proton conductivity within a hydrogen-bonded organic framework. *Angew. Chem. Int. Ed.* **62**, e202308418 (2023).
45. Zhang, A.-A., Wang, Z.-X., Fang, Z.-B., Li, J.-L. & Liu, T.-F. Long-range π-π stacking brings high electron delocalization for enhanced photocatalytic activity in hydrogen-bonded organic framework. *Angew. Chem. Int. Ed.* **63**, e202412777 (2024).
46. Yin, Q. et al. Metallization-prompted robust porphyrin-based hydrogen-bonded organic frameworks for photocatalytic CO_2 reduction. *Angew. Chem. Int. Ed.* **61**, e202115854 (2022).
47. Yu, B. et al. Robust biological hydrogen-bonded organic framework with post-functionalized rhenium(I) sites for efficient heterogeneous visible-light-driven CO_2 reduction. *Angew. Chem. Int. Ed.* **60**, 8983–8989 (2021).
48. Gao, X. Y. et al. Recent advancements of photo- and electro-active hydrogen-bonded organic frameworks. *Sci. China Chem.* **65**, 2077–2095 (2022).
49. Lu, C. J. et al. Modulating the microenvironments of robust metal hydrogen-bonded organic frameworks for boosting photocatalytic hydrogen evolution. *Angew. Chem. Int. Ed.* **63**, e202405451 (2024).
50. Zhang, Y. et al. H_2O_2 generation from O_2 and H_2O on a near-infrared absorbing porphyrin supramolecular photocatalyst. *Nat. Energy* **8**, 361–371 (2023).
51. Wan, X.-J., Li, C. X., Zhang, M. T. & Chen, Y. S. Acceptor-donor-acceptor type molecules for high performance organic photovoltaics-chemistry and mechanism. *Chem. Soc. Rev.* **49**, 2828–2842 (2020).
52. Chen, X., Zhang, X., Xiao, X., Wang, X. & Zhao, J. Z. Recent developments on understanding charge transfer in molecular electron donor-acceptor systems. *Angew. Chem. Int. Ed.* **62**, e202216010 (2023).
53. Yang, C., Cheng, B., Xu, J. S., Yu, J. G. & Cao, S. W Donor-acceptor-based conjugated polymers for photocatalytic energy conversion. *EnergyChem* **6**, 100116 (2024).
54. Xu, H. et al. Programming tetrathiafulvalene-based covalent organic frameworks for promoted photoinduced molecular oxygen activation. *Angew. Chem. Int. Ed.* **63**, e202405476 (2024).
55. Gao, X.-Y., Li, Y.-L., Liu, T.-F., Huang, X.-S. & Cao, R. Single-crystal-to-single-crystal transformation of tetrathiafulvalene-based hydrogen-bonded organic frameworks. *CrystEngComm* **23**, 4743–4747 (2021).
56. Zheng, X. M. et al. Hydrogen bonded-directed pure organic frameworks based on TTF-tetrabenzoic acid and bipyridine base. *Synth. Met.* **263**, 116365 (2020).
57. Luo, Y.-H. et al. A dynamic 3D hydrogen-bonded organic frameworks with highly water affinity. *Adv. Funct. Mater.* **28**, 1804822 (2018).
58. Zhang, X. et al. Developing Ni single-atom sites in carbon nitride for efficient photocatalytic H_2O_2 production. *Nat. Commun.* **14**, 7115 (2023).
59. Kofuji, Y. et al. Carbon nitride-aromatic diimide-graphene nanohybrids: metal-free photocatalysts for solar-to-hydrogen peroxide energy conversion with 0.2% efficiency. *J. Am. Chem. Soc.* **138**, 10019–10025 (2016).
60. García-Serna, J. et al. Engineering in direct synthesis of hydrogen peroxide: targets, reactors and guidelines for operational conditions. *Green Chem.* **16**, 2320 (2014).
61. Mase, K., Yoneda, M., Yamada, Y. & Fukuzumi, S. Seawater usable for production and consumption of hydrogen peroxide as a solar fuel. *Nat. Commun.* **7**, 11470 (2016).
62. Lu, J. N. et al. Synergistic metal-nonmetal active sites in a metal-organic cage for efficient photocatalytic synthesis of hydrogen peroxide in pure water. *Angew. Chem. Int. Ed.* **62**, e202308505 (2023).
63. Chen, S. Y. et al. Identification of the highly active Co-N_4 coordination motif for selective oxygen reduction to hydrogen peroxide. *J. Am. Chem. Soc.* **144**, 14505–14516 (2022).
64. Kou, M. P. et al. Molecularly engineered covalent organic frameworks for hydrogen peroxide photosynthesis. *Angew. Chem. Int. Ed.* **61**, e202200413 (2022).
65. Shi, X. J. et al. Understanding activity trends in electrochemical water oxidation to form hydrogen peroxide. *Nat. Commun.* **8**, 701 (2017).
66. Zhou, Z. M. et al. A thioether-decorated triazine-based covalent organic framework towards overall H_2O_2 photosynthesis without sacrificial agents. *Appl. Catal. B Environ. Energy* **334**, 122862 (2023).
67. Luo, Y. et al. Sulfone-modified covalent organic frameworks enabling efficient photocatalytic hydrogen peroxide generation via

one-step two-electron O_2 reduction. *Angew. Chem. Int. Ed.* **62**, e202305355 (2023).
68. Wang, H. Z., Yang, C., Chen, F. S., Zheng, G. F. & Han, Q. A crystalline partially fluorinated triazine covalent organic framework for efficient photosynthesis of hydrogen peroxide. *Angew. Chem. Int. Ed.* **61**, e202202328 (2022).
69. Zhao, C. et al. Molecular level modulation of anthraquinone-containing resorcinol-formaldehyde resin photocatalysts for H_2O_2 production with exceeding 1.2 % efficiency. *Angew. Chem. Int. Ed.* **62**, e202218318 (2023).
70. Cheng, H. et al. Rational design of covalent heptazine frameworks with spatially separated redox centers for high-efficiency photocatalytic hydrogen peroxide production. *Adv. Mater.* **34**, 2107480 (2022).
71. Chen, Z. et al. Tuning excited state electronic structure and charge transport in covalent organic frameworks for enhanced photocatalytic performance. *Nat. Commun.* **14**, 1106 (2023).
72. Cheng, J. et al. Fully conjugated 2D sp^2 carbon-linked covalent organic frameworks for photocatalytic overall water splitting. *Adv. Mater.* **36**, 2305313 (2024).
73. Cheng, M. et al. Nitrogen-doped carbonized polyaniline (N-CPANI) for peroxydisulfate (PDS) activation towards efficient degradation of doxycycline (DOX) via the non-radical pathway dominated by electron transfer. *Chem. Eng. J.* **453**, 139810 (2023).
74. Tang, S., Yin, X., Wang, G., Lu, X. & Lu, T. Single titanium-oxide species implanted in 2D g-C_3N_4 matrix as a highly efficient visible-light CO_2 reduction photocatalyst. *Nano Res.* **12**, 457–462 (2019).

Acknowledgements

D.-C.Z. is thankful for the National Natural Science Foundation of China (22271218), and the Key Project of Tianjin Natural Science Foundation (24JCZDJC00220). T.-B.L. is thankful for the National Key R&D Program of China (2022YFA1502902). Z.-M.G. thanks the Tianjin University of Technology Innovation Project for Postgraduate Students (YJ2396).

Author contributions

D.-C.Z. conceived and designed the study. J.-H.Z. and Z.-M.G. performed the experiments. J.W. operated the DFT calculation. J.-H.Z., Z.-M.G., J.W., D.-C.Z. and T.-B.L. analyzed the data. D.-C.Z. supervised the experiments. J.-H.Z. and D.-C.Z. co-wrote the paper.

Competing interests

The authors declare no competing interests.

Additional information

Supplementary information The online version contains supplementary material available at https://doi.org/10.1038/s41467-025-57939-8.

Correspondence and requests for materials should be addressed to Di-Chang Zhong.

Peer review information *Nature Communications* thanks Hangxun Xu and the other, anonymous, reviewers for their contribution to the peer review of this work. A peer review file is available.